Xue et al. *Microsystems & Nanoengineering* (2025)11:75
https://doi.org/10.1038/s41378-025-00935-1

Microsystems & Nanoengineering
www.nature.com/micronano

ARTICLE Open Access

A high-performance 10 mm diameter MEMS fast steering mirror with integrated piezoresistive angle sensors for laser inter-satellite links

Wenli Xue[1,2], Yichen Liu[1,2], Xingwang Zhu[3], Mingkun Wang[4], Zhichao Weng[3,5], Yongquan Su[1], Yi Yang[3,6], Hongfeng Zhao[3,5], Yang Wang[1,2], Hao Chen[1,2], Lihao Wang[1,4]✉ and Zhenyu Wu[1,2,3,4,5]✉

Abstract

This paper presents a compact and high-performance piezoelectric micro-electro-mechanical system (MEMS) fast steering mirror (FSM) designed for use in laser inter-satellite links (ISLs). The FSM features a large optical aperture of 10 mm and is batch fabricated using an 8-inch wafer-level eutectic bonding process, packaged into a volume of $26 \times 22 \times 3$ mm^3. Notably, the piezoresistive (PZR) sensor is integrated on the spring of the FSM to facilitate precise beam control. Furthermore, an intermediate directional defect structure is novelly designed to create a Stress Concentration Region (SCR), effectively improving PZR sensitivity from 3.3 mV/(V·mrad) to 5.4 mV/(V·mrad). In this article, various performance metrics of the FSM are tested, including the mechanical characteristics, PZR sensor properties, and mirror optical quality, which all meet the requirements for laser ISLs. Results indicate that the FSM achieves a high resonant frequency (>1 kHz) and a low nonlinearity of 0.05%@ ± 2.1 mrad. A remarkable minimum angular resolution of 0.3 μrad and a repeated positioning accuracy of 1.11 μrad ensure exceptional pointing precision. The open-loop control is driven by the double-step algorithm, resulting in a step response time of 0.41 ms and achieving a control bandwidth over 2 kHz. Additionally, the integrated angular sensor demonstrates a nonlinearity of 0.09%@ ± 1.05 mrad, a sensitivity of 5.1 mV/(V·mrad), and a minimum angular resolution of 0.3 μrad. Under quasi-static driven conditions (500 Hz @ ± 2 mrad), the maximum dynamic deformation of the mirror surface is merely 2 nm.

Introduction

In recent years, the development of inter-satellite links (ISLs) has attracted significant attention due to the increasing demand for space communication. ISLs enable high-speed data transfer between satellites, greatly enhancing the overall performance and flexibility of satellite networks[1]. Laser communication technology is recognized as a key enabler for efficient ISLs, offering advantages such as higher communication capacity, wider spectrum bandwidth, lower power consumption, and enhanced resilience to interference compared with radio frequency (RF) communication[2]. Currently, satellite constellations such as Starlink, SLILEX, LCTSX, G60, and China SatNet have already adopted laser ISLs as one of their core transmission methodologies. Laser communication terminals are anticipated to become standard communication equipment in future spacecraft payloads.

However, achieving extremely precise beam pointing poses a significant challenge in the implementation of ISLs. The pointing, acquisition, and tracking (PAT) system is a core module for optical communications between satellites and between satellite and Earth[3,4]. A fast steering mirror (FSM) with high precision and optical quality is essential to the PAT system, functioning as the core device for achieving accurate beam steering in current state-of-the-art solutions[5].

Correspondence: Lihao Wang (lhwang@mail.sim.ac.cn) or Zhenyu Wu (zhenyu.wu@mail.sim.ac.cn)
[1]State Key Laboratory of Transducer Technology, Shanghai Institute of Microsystem and Information Technology, Chinese Academy of Sciences, Shanghai, China
[2]University of Chinese Academy of Sciences, Beijing, China
Full list of author information is available at the end of the article

Traditional FSMs are typically actuated using voice coil motors or piezoelectric ceramics. Voice coil motor-based FSMs generate driving force using magnetic fields, providing significant stroke lengths, low driving voltages, and high load capacities that enhance reliability. However, these systems need improved magnetic shielding and have limited operational frequencies, which may affect their robustness[6]. Piezoelectric ceramic FSMs leverage the inverse piezoelectric effect of bulk piezoelectric materials, such as PZT, to generate a driving force. While they offer strong driving force and quick response time, PZT faces challenges with impact resistance and reliability. Additionally, PZT's hysteresis requires complex driving circuits and compensation algorithms. The larger size and weight of traditional FSMs render them unsuitable for compact satellite platforms, complicating miniaturization efforts and increasing launch costs, thereby limiting mass production potential in commercial applications[7]. Recently, an increasing number of research institutions have begun utilizing commercial off-the-shelf (COTS) MEMS FSMs to construct their systems. Due to their low cost, small size, light weight, and low power consumption, the MEMS FSMs hold significant application potential in laser ISLs. For example, many institutions use an electrostatic comb-drive MEMS FSM from Mirrorcle Technologies. The CubeSat laser infrared crosslink (CLICK) mission is a technology demonstration for CubeSat optical communication terminals, focusing on downlinks and crosslinks[8,9]. The CLICK-A 1.2U downlink terminal employs a 5 mm MEMS FSM. The results showed that the MEMS FSM was able to correct an average blind spacecraft pointing of 8.494 mrad and maintain an average RMS pointing error of 0.175 mrad after initial blind pointing error correction. Another CubeSat laser downlink demonstration mission, developed at the MIT Space Telecommunications, Astronomy, and Radiation Laboratory[10], used a 3.6 mm MEMS FSM. Experimental results showed that beacon tracking errors of only 16 µrad RMS are feasible for both axes. The satellite team of the Stanford Student Space Initiative (SSI) designed and built the Polar-Orbiting Infrared Tracking Receiver (POINTR), a 1U CubeSat payload aimed to demonstrate optical-communications technology. A 4.2 mm gold-plated MEMS FSM was used on their 1U terminal and received a 0.5° tracking FOV[11]. The Aerospace Corporation (El Segundo, USA) let their design fit within 1U with a 6.4 mm diameter MEMS FSM, which enables minimization of SWaP in the laser communication terminal, which is crucial in CubeSat laser communications. The prototype was designed such that it has an acquisition FOV of 2° and tracking FOV of 0.5°, with an acquisition time measured at less than 60 s and a success probability exceeding 99%[5]. These four institutions mentioned above all used COTS MEMS FSMs from Mirrorcle Technologies. Besides these, an electromagnetically driven 3 mm Hamamatsu S1227-03P MEMS FSM was used by the Laboratory of Lean Satellite Enterprises and In-Orbit Experiments (LaSEINE) in Japan to stabilize a laser communication link on an optical bench in the laboratory. In the closed-loop mode, they used a photodiode array PDA sensor to receive stabilization for over 20 s despite the induced fluctuations by the vibration machine[12]. Furthermore, closed-loop control can provide more stable and precise beam control, thereby improving system tracking accuracy. However, existing COTS MEMS FSMs generally lack integrated sensors, and some research institutions rely on external sensors, such as the beacon detector[10], consisting of a focal plane array (FPA) and a focusing lens assembly (LA), and the PDA sensor[12], to construct closed-loop control systems. These approaches not only increase the overall size of the system but also lead to higher costs. Consequently, current COTS MEMS FSMs are not designed for the specific requirements of laser ISLs, exhibiting several shortcomings such as small mirror sizes, low frequency, and the lack of integrated sensors.

To meet the requirements of laser ISLs, the key criteria of an FSM include[13]: (1) size, weight, and power (SWaP): SWaP is the critical constraint for compact satellite platforms. The mass of FSMs typically ranges from a few grams to several kilograms, depending on the technology used and the dimensions of the mirror. Minimizing component size contributes to a more compact laser terminal, facilitating miniaturization and reducing satellite launch costs; (2) optical/mechanical steering angles: the mechanical steering angle of the mirror refers to its angular deviation from a reference position. A larger steering angle provides significant advantages for both the transmitter and receiver by expanding the field of view (FOV) necessary for effective tracking. The mechanical angle requirements for FSM in laser ISLs need to achieve at least ±1.5 mrad; (3) operational bandwidth: the operational bandwidth of the FSM indicates its responsiveness to control signals and its capacity for rapid positional adjustments. For instance, the bandwidth criteria for FSM are closely linked to satellite oscillations[14]. Typically, the required bandwidths for an FSM range from several hundred Hz to over 1 kHz; (4) pointing accuracy: pointing accuracy is an important measure that depends on the resolution and repeatability of an FSM, which is vital for long-distance laser ISLs. Additionally, an angle sensor can provide real-time monitoring of mirror deflection angles, enabling more precise beam control through closed-loop systems. The current state-of-the-art fine beam pointing systems have pointing accuracies ranging from ±48 µrad to ±0.48 µrad[15,16]; (5) mirror surface quality: the quality of the mirror surface, characterized by measures such as root mean square (RMS) and peak-to-valley (PV)

displacements, must be minimized to ensure optimal performance. For laser ISLs, the requirement is RMS < λ/20 at λ = 1550 nm.

This study focuses on the development of a high-performance, compact MEMS FSM with a diameter of 10 mm, specifically designed for laser ISLs. It integrates an on-chip, high-sensitivity piezoresistive (PZR) sensor element to achieve more precise beam control. The structure of this paper is as follows: section "Design concept" provides the design and simulation results of the mechanical structure. It also discusses the design principles of the PZR structure and optimization strategies for sensitivity. Section "Fabrication" details the fabrication process for the MEMS FSM. Section "Results and discussion" presents the characterization results of the MEMS FSM, including mechanical performance, repeatability accuracy, control bandwidth, piezoresistive performance, and the dynamic deformation of the mirror surface. Additionally, at the end of this section, we perform a comparative analysis between various FSMs and the device presented in this study. Ultimately, in the section "Conclusion", the research findings are summarized, and potential directions for future optimization are suggested.

Design concept

This study aims to develop a high-performance MEMS FSM specifically designed for laser ISLs. By optimizing the mechanical structure, this design achieves a high resonant frequency, meeting the requirement for laser ISLs above 1 kHz. In addition, while maintaining a mirror plate of 10 mm, the chip size has been significantly reduced[17], increasing the fill factor. This makes the device particularly well-suited for compact satellite platforms and leads to a reduction in launch costs, making it an economically viable option for space applications. In addition, an innovative stress concentration structure is designed to improve the sensitivity of the integrated PZR sensors, enabling more precise beam control.

Design of the device structure

To achieve a higher fill factor and resonant frequency, this design uses a double-layered stacked structure similar to that described in our previous work[17,18]. The MEMS FSM consists of two parts: the actuator and the mirror. The actuator layer consists of a frame, cantilevers, springs, and a support pillar. Two pairs of cantilevers are connected to the support pillar via springs. Additionally, the support pillar is joined to the center of the 10 mm mirror plate through a wafer-level bonding process, which facilitates precise alignment and enhances structural reliability. Notably, this structure magnifies the deflecting angle of the mirror by the leverage principle.

Piezoelectric thin films are compatible with semiconductor processes, and we choose Sc-doped AlN (AlScN) film as the driving material. Although PZT has a higher piezoelectric coefficient, its hysteresis property brings a nonlinearity problem, and prolonged exposure to an electric field can lead to fatigue, adversely affecting the long-term stability of devices. The AlN film has high linearity and high reliability, but the piezoelectric coefficient is too low to satisfy the requirement of large deformation under the quasi-static operation of FSM. Therefore, in this work, AlScN film is used as the driving material, which has a higher piezoelectric coefficient along with the advantages of AlN. The AlScN film we use is doped with 20% of Sc element[19].

The optimization of the spring structure, in conjunction with finite element analysis (FEA) simulations, has led to an increased resonant frequency and a significant reduction in chip size, which meets the requirement for the laser ISLs. Figure 1a shows the simulation structure of the MEMS FSM with a 10 mm circular optical aperture. The fixed support point is the anchor point of the cantilever beam that connects to the frame. Figure 1b–d show the FEA simulation results for the first three vibrational modes. The first mode is the tip/tilt mode of two axes with a frequency of 1253 Hz. The third mode of the MEMS FSM is the piston mode at 2827 Hz, which is increased to higher than 2 kHz. This enhancement effectively minimizes the susceptibility to critical resonant frequencies in the ambient random vibrations ranging from 20 Hz to 2000 Hz, thereby improving the device's reliability under such conditions[20]. Furthermore, simulations of the tilting angle indicate that the maximum tilting angle of the mirror reaches 2 mrad at an applied voltage of 90 V.

Design of the piezoresistive sensor

As shown in Fig. 1e, the PZR sensor is a Wheatstone bridge consisting of four piezoresistive bars, which are strategically positioned on the spring of the FSM. When the FSM tilts, the spring connecting the cantilever beam and the pillar experiences considerable normal stress. This stress induces deformation within the piezoresistive elements, leading to a change in their resistivity, which subsequently alters the output voltage of the bridge circuit. The normal stress at the piezoresistive position is directly proportional to the FSM's tilting angle. Consequently, this relationship allows for real-time monitoring of the FSM's position through variations in the output voltage of the Wheatstone bridge.

The FSM employs P-type PZRs, and the maximum output voltage of the PZRs can be achieved when both the cantilever beam and PZRs are oriented along the <110> crystal direction. The formula for calculating the bridge

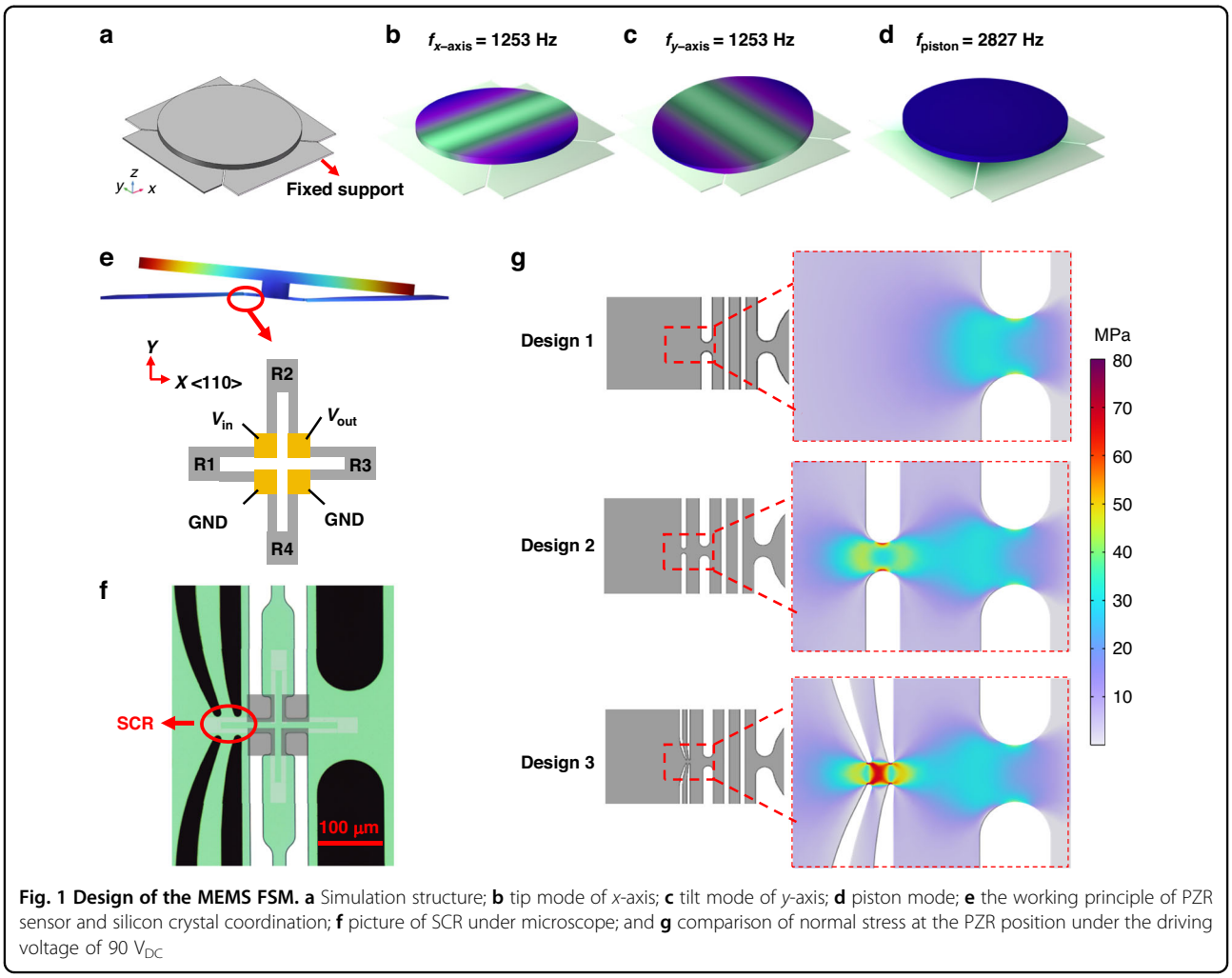

Fig. 1 Design of the MEMS FSM. a Simulation structure; **b** tip mode of *x*-axis; **c** tilt mode of *y*-axis; **d** piston mode; **e** the working principle of PZR sensor and silicon crystal coordination; **f** picture of SCR under microscope; and **g** comparison of normal stress at the PZR position under the driving voltage of 90 V_{DC}

output voltage is provided in the following expression:

$$V_{output} = \left(\frac{R3}{R2+R3} - \frac{R4}{R1+R4}\right) V_{input} = \left(\frac{1+\frac{\Delta R3}{R3}}{2+\frac{\Delta R2}{R2}+\frac{\Delta R3}{R3}} - \frac{1+\frac{\Delta R4}{R4}}{2+\frac{\Delta R1}{R1}+\frac{\Delta R4}{R4}}\right) V_{input} \quad (1)$$

V_{input} is the supply voltage, $\frac{\triangle R}{R}$ is the change in resistance of the PZRs at each position, expressed as:

$$\frac{\triangle R}{R} = \pi_{l,110}\sigma_l + \pi_{t,110}\sigma_t \quad (2)$$

$\pi_{l,110}$ and $\pi_{t,110}$ are the longitudinal and transverse piezoresistive coefficients of the PZRs oriented along the <110> crystal direction. σ_l and σ_t are the longitudinal and transverse stresses acting on the PZR position. For P-type PZRs with a doping concentration of 1e19 cm^{-3}, $\pi_{l,110} = 43\times10^{-11}Pa^{-1}$ and $\pi_{t,110} = -40\times10^{-11}Pa^{-1}$[21]. Specifically, at a doping concentration of 1e19 cm^{-3}, the piezoresistive coefficient declines to 60% of its standard value[21]. The temperature coefficient of resistance (TCR) attains a relatively low value[22].

High-sensitivity piezoresistive sensors can yield greater voltage output under the same micro-mirror rotation angle, enhancing the angular resolution of the PZRs and enabling more precise beam control. The expression for PZR sensor sensitivity is given as:

$$S = \frac{V_{output}}{V_{input} * \theta_{mech}} \quad (3)$$

θ_{mech} is the mechanical steering angle of the FSM. To enhance the sensitivity of the PZRs while maintaining the same supply voltage and doping concentration, it is essential to increase the stress experienced at the PZR position when the FSM tilts. In this study, a novel intermediate directional defect structure is designed at the front end of the cantilever beam. Figure 1f depicts a micrograph of the PZR position. Four long and narrow slots are etched to create a stress concentration region

(SCR). Here, we give three different structures at the PZR position. Figure 1g presents the stress simulation results at the PZR position under a tilting angle of the FSM at 2 mrad. Design 1 represents the baseline structure without SCR, with only relatively high stress appearing at the narrow spring position of R3. Design 2 has two etched slots, concentrating stress at the position of R2 in addition to the position of R3. As shown in the figure, the stress distribution at the position of R2 appears smaller in the middle and larger on the sides. Following further optimization, Design 3 introduces four slots, whose orientations are pointed to the middle, concentrating stress entirely at the position of the central PZR (R2), maximizing the PZR sensitivity. Additionally, maximizing the longitudinal length of the slots and minimizing the gap width between the four slots results in the maximum stress. Considering the precision of the fabrication process, the arrangement of PZRs, and the design of electrical connections, the present Design 3 is optimal for achieving enhanced sensitivity. Table 1 provides the transverse and longitudinal stress magnitudes at the PZR position for the three designs, along with the calculated PZR sensitivity, showing a 63% improvement for Design 3 compared to the initial design. Theoretically, the piezoresistive sensitivity of Design 3 is 5.4 mV/(V·mrad).

Fabrication

The PZR-integrated MEMS FSM utilizes an SSD (SOI-based Single piezoelectric layer Double release)-FSM process consisting of two layers: an AlScN actuator wafer and a mirror plate wafer. The AlScN actuator wafer starts with an SOI wafer with a 500 μm handle layer, a 1 μm buried oxide layer, and a 100 μm device layer. The choice of a 100 μm top silicon thickness is based on the maturity of current manufacturing processes for SOI wafers with this specification. Additionally, given the large dimensions of our mirrors and the design requirement to exceed 1 kHz, we did not choose thinner top silicon layers to ensure structural performance. The mirror plate wafer needs an SOI wafer with a 450 μm handle layer, a 1 μm buried oxide layer, and a 50 μm device layer. This configuration is chosen to balance both the mirror surface profile and mass, ensuring that the surface quality meets the requirement while minimizing its weight, which is crucial for achieving higher resonant frequencies. The process used for its fabrication, which is suitable for 8-inch mass production, is depicted in Fig. 2a. The fabrication process of the actuator layer is divided into five main steps: (1) firstly, a 50 nm thick silicon oxide layer is thermally oxygenated on the surface. Then, the p-type piezoresistive sensors are formed by boron ion injection and thermally annealed, and the doping concentration of the piezoresistive sensors is $1\times 10^{19}/\mathrm{cm}^3$. However, due to the relatively low doping concentration of boron ions, further boron ion implantation is required for better subsequent ohmic contacts. (2) The upper electrode Mo (200 nm), the piezoelectric layer AlScN (1.5 μm), and the lower electrode Mo (200 nm) were deposited on top of the oxide layer by magnetron sputtering and patterned. (3) On the top Mo layer, 500 nm silicon oxide is deposited by the PECVD (plasma enhanced chemical vapor deposition) process as a passivation layer and then dry-etched by RIE (Reactive Ion Etching) to form the electrical contact via. After that, a 1 μm Al layer is deposited by magnetron sputtering on the wafer and patterned to form electrical connections. Since the pads are patterned simultaneously during this step, maximizing the thickness of the Al layer is essential. Furthermore, we select Al due to its cost-effectiveness compared to gold, making it a practical choice for our device. (4) The 100 μm device layer is patterned by DRIE (Deep Reactive Ion Etching) to form the actuators and springs. Then, a 500 nm Al layer is deposited by magnetron sputtering on the backside of the handle layer as a bonding metal. For the bonding metal, Al-Ge provides a robust mechanical connection between wafers. The bond strength is critical for ensuring reliability under dynamic forces and vibrations experienced by the FSM. (5) The bonding metal and the handle layer are patterned and etched by DRIE from the back side to release all the movable parts of the device. The fabrication process of the mirror layer is divided into three main steps: (6) a 500 nm Ge layer is sputtered on the bottom

Table 1 Piezoresistive sensitivity comparison of three designs

	Design 1		Design 2		Design 3	
	σ_l (Mpa)	σ_t (Mpa)	σ_l (Mpa)	σ_t (Mpa)	σ_l (Mpa)	σ_t (Mpa)
R1	8	−6	27	3	49	−4
R2	−5	3	−5	6	−6	3
R3	29	−4	28	5	26	−6
R4	−5	3	−5	6	−6	3
Sensitivity (mV/(V·mrad))	3.3		3.6		5.4	

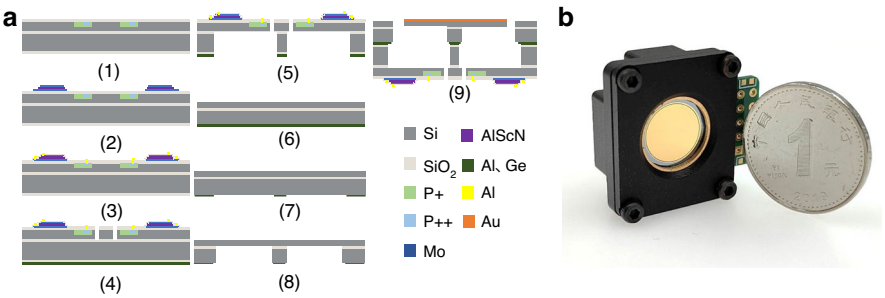

c

Parameter	Value
Volume	26 mm × 22 mm × 3 mm
Aperture	10 mm
Actuator thickness	100 μm
Mirror thickness	500 μm
Tip/tilting mode frequency	1253 Hz
Piston mode frequency	2827 Hz
Mechanical tilting angle @ ±90 V_{DC}	±2 mrad

Fig. 2 Fabrication process of the MEMS FSM. a Fabrication process flow of MEMS FSM; **b** photograph of the packaged MEMS FSM; and **c** design parameters of MEMS FSM

silicon as the bonding layer. (7) The Ge layer is patterned for next eutectic bonding. (8) A honeycomb-shaped reinforcement structure was patterned and etched into the bottom silicon by DRIE to reduce the mass and strengthen the stiffness of the mirror plate. (9) Bond the mirror plate wafer to the actuator wafer and release the mirror. Notably, the dual-face alignment during the bonding process presents a significant challenge. During the manual alignment process, a microscope is employed to verify alignment accuracy. Finally, Au is magnetron sputtered as the mirror reflective layer. Figure 2b gives the photograph of the packaged MEMS FSM, and Fig. 2c summarizes the final parameters of the MEMS FSM.

Results and discussion

After completing the fabrication of the device, we characterize the basic mechanical properties (including resonance frequency, mechanical tilting angle, nonlinearity, and angular resolution), pointing accuracy, open-loop control performance (including step response, operational bandwidth, and stability), PZR performance (including sensitivity, nonlinearity, stability, and angular resolution) and the dynamic deformation of the mirror.

Performance test platform

Figure 3a, b gives the position sensitive detectors (PSD) test schematic and the built test platform. The laser emitted by the laser source is reflected by the mirror plate and received by the PSD, which records the position of the laser spot. When the driving signal generated by the computer acts on the MEMS FSM through the data acquisition card, the mirror will tilt, resulting in a change in the position of the laser spot. This positional change is then calculated to determine the tilting angle of the MEMS FSM and recorded by the computer. The PSD exhibits a rapid response speed and enhanced temporal resolution, resulting in superior performance in tests that require quick and sensitive dynamic responses.

However, PSD is sensitive to variations in ambient light and temperature, resulting in high levels of noise (>10 μrad). To achieve a more accurate characterization of the angular resolution of the FSM and pointing accuracy, a collimator test system shown in Fig. 3c, d is constructed. The background noise of the system is only 0.2 μrad. The collimator directs a collimated beam of light towards the mirror. As the mirror is actuated and deflecting, it alters the direction of the reflected beam. A detection system analyzes the deviation of the reflected beam. By calculating the change in beam position relative to the initial alignment, the tilting angle of the FSM can be accurately determined and recorded by the computer.

The basic mechanical performance

Initially, we characterize the basic mechanical performance of the FSM. As shown in Fig. 4a, the frequency response is assessed using laser Doppler velocimetry (LDV), revealing resonant frequencies of 1231.2 Hz for the x-axis and 1228.1 Hz for the y-axis, which are

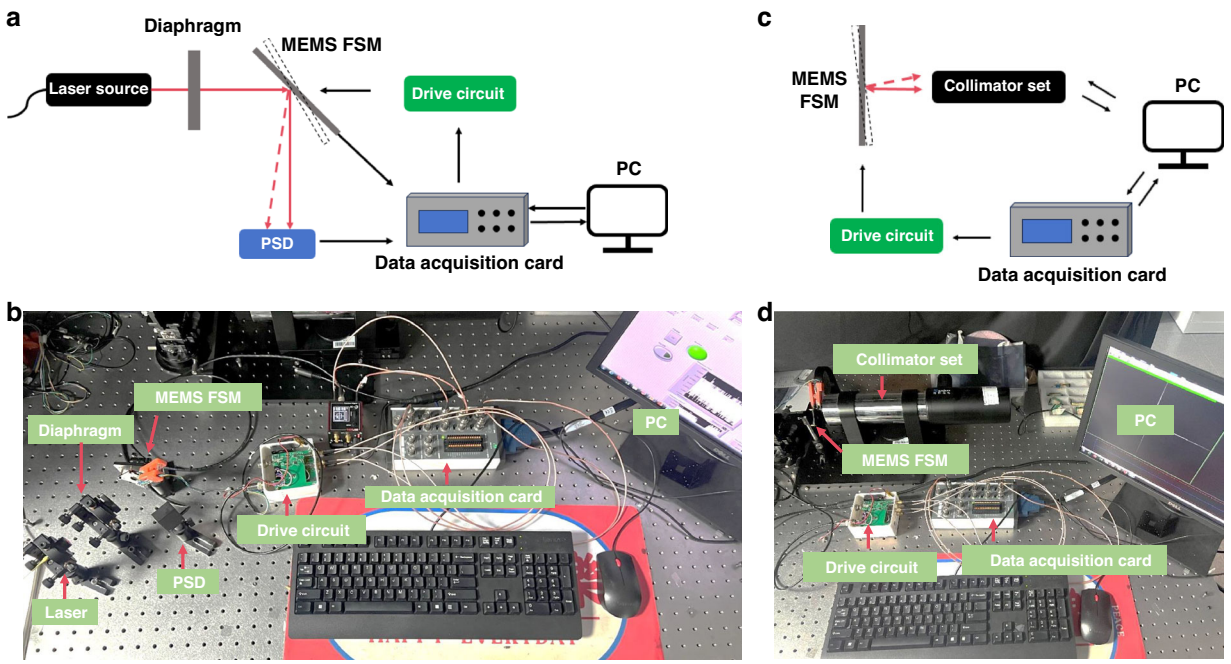

Fig. 3 The test schematic and the built test platform. a Schematic diagram of the PSD test platform; **b** the built PSD test platform; **c** schematic diagram of the collimator test platform; and **d** the built collimator test platform

consistent with the simulation results. To evaluate the mechanical tilting angle and nonlinearity of the FSM, a sequence of direct current (DC) voltages ranging from −110 V to +110 V, with an increment of 11 V each step, is applied. Figure 4b shows that the nonlinearities of the *x*-axis and *y*-axis measure 0.04%@ ± 2.16 mrad and 0.05% @ ± 2.18 mrad, which is the full-scale, the maximum driving voltage that our piezoelectric film can withstand, of the device. The nonlinearity of both axes is smaller than 0.1%, ensuring the pointing accuracy for the FSM. Additionally, the angular resolution of the FSM is tested, which is also a critical parameter for pointing accuracy. Figure 4c, d shows the angular resolution results obtained using the collimator testing system. A step wave is used for driving, wherein each voltage was held for 0.5 s while recording data at a rate of 100 points per second. It can be observed that the minimum angular resolution of the FSM, which can be tested under the current test platform, is 0.3 μrad @ 16.5 mV. However, at a lower driving voltage of 13.75 mV, likely due to either the noise inherent in the testing system or limitations associated with the device itself, a smaller angular resolution could not be obtained. Such high precision is critical for maintaining accurate pointing and tracking capabilities, which ensure effective communication in dynamic environments.

Pointing accuracy

In addition to nonlinearity and angular resolution, the repeatability of the FSM is another critical metric for assessing its pointing accuracy. In Fig. 4e, a voltage of +55 V, +27.5 V, 0 V, −27.5 V, and −55 V is applied to both axes, randomly sampling positions in a 5× 5 grid and repeating this process 32 times. By zooming in on one point, it can be observed that: thirty-two points are randomly distributed over a small range, 1.5 μrad in the *x* direction and 2 μrad in the y direction. This distribution encompasses fluctuations attributed to the system error of 0.2 μrad. To further quantify the repeatability of the FSM, the voltage is cycled from 0 V to −55 V, −44 V, …, 55 V back and forth 32 times for each target voltage. Whenever returning to 0 V, we record the tilting angle and the triple standard deviation (3σ) of the 32 measurements is calculated as shown in Fig. 4f. The maximum value of 3σ at different voltages is defined as the zero-point repeatability, yielding values of 1.11 μrad for the *x*-axis and 1.05 μrad for the *y*-axis. Similarly, in Fig. 4g, the voltage is cycled from 0 V to −55 V, −44 V, …, 55 V back and forth 32 times for each target voltage. Whenever reaching the target voltage, we record the tilting angle, and the 3σ of 32 measurements is calculated. The maximum value of the 3σ at different voltages is defined as repeatable positioning accuracy, resulting in values of 1.09 μrad for the *x*-axis and 1.04 μrad for the *y*-axis. This analysis underscores the FSM's capability to achieve precise angular positioning.

Open-loop control performance

To measure the open-loop step response of the MEMS FSM, a step voltage is applied to drive the mirror. As

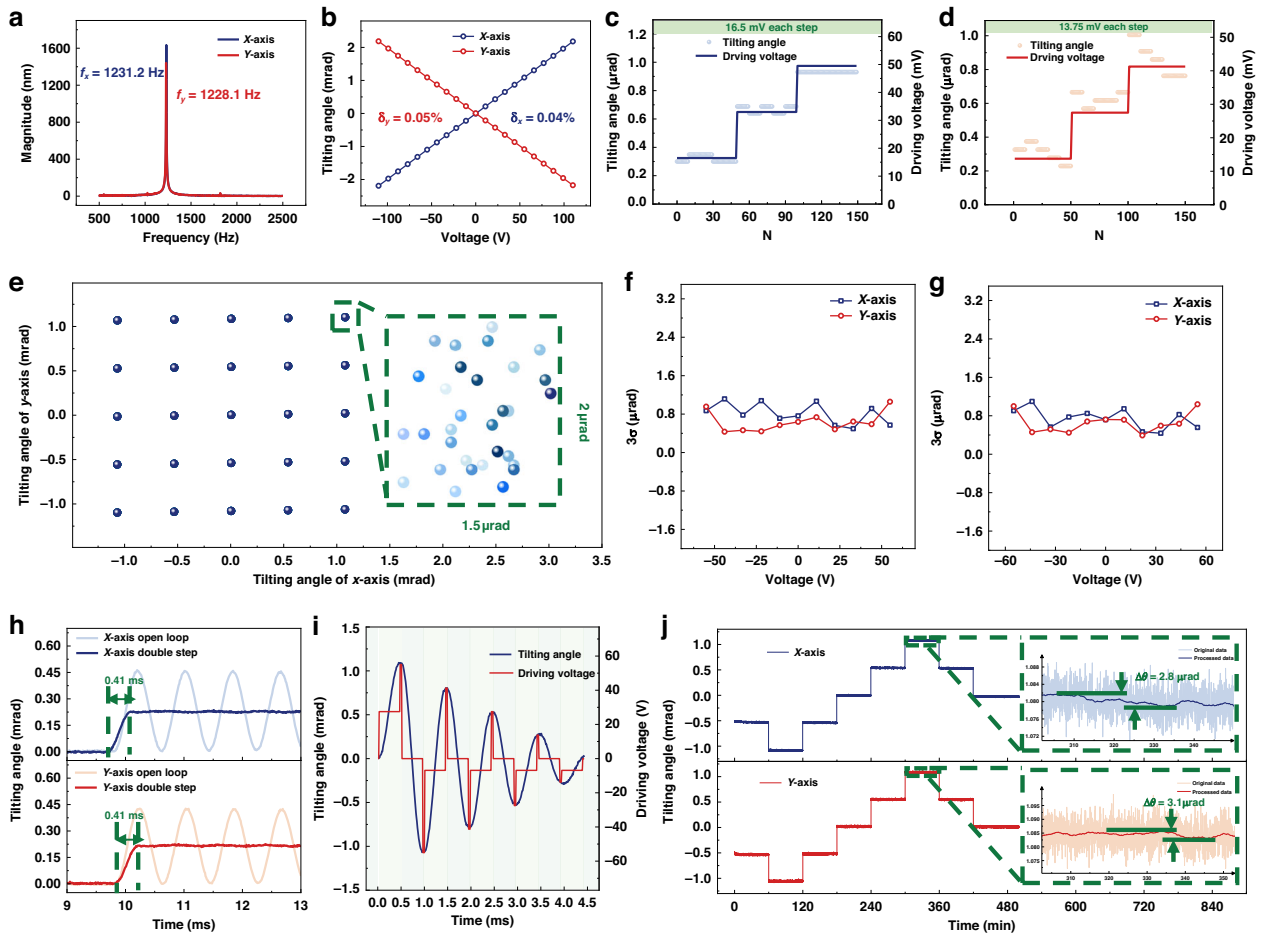

Fig. 4 The open-loop test results of the MEMS FSM. a Resonant frequency of two axes; **b** tilting angle linearity of two axes at full scale (±110 V); **c** angular resolution at 16.5 mV each step; **d** angular resolution at 13.75 mV each step; **e** two-dimensional sweep repeatability; **f** repeatability of zero position of two axes; **g** tilting angle repeatability of two axes; **h** step response of two axes; **i** maximum operational bandwidth; and **j** tilting angle stability of two axes

depicted in Fig. 4h, the maximum overshoots for both axes exceed 100%, and the settling time of the step response is long under open-loop control. Therefore, a double-step feedforward control algorithm is applied to the device and the step response performance of the device. The overshoot is sharply decreased, and the settling time is only 0.41 ms. Thus, an open-loop operational bandwidth of more than 2000 Hz can be obtained through the feedforward control algorithm[23]. In Fig. 4i the *x*-axis is actuated using the feedforward control algorithm. The red line in the figure represents the driving voltage, which is a step voltage that changes upon the mirror reaching the desired angle. Throughout the experiment, nine distinct target voltages were utilized: ±55 V, ±41.25 V, ±27.5 V, ±13.75 V, and 0 V, with a control cycle of 0.48 ms. A control bandwidth of 2083 Hz is achieved. The high-frequency response of FSMs allows for real-time compensation of the oscillations experienced by satellites, ensuring that the laser beam remains accurately directed at the target. Figure 4j characterizes the stability of the device by independently driving each axis through a sequence of voltages: −27.5 V, −55 V, −27.5 V, 0 V, 27.5 V, and 55 V, maintaining each voltage for 1 h. Under a driving voltage of 55 V, the maximum fluctuation observed within this hour was 2.8 μrad for the *x*-axis and 3.1 μrad for the *y*-axis. The high stability is critical for ensuring the accuracy of the overall system performance.

PZR sensor performance

The integrated PZR sensors have the potential to enhance the mirror's performance in laser ISLs by providing more precise beam control, real-time feedback, and the ability to compensate for external disturbances, ultimately leading to more reliable and efficient communication systems. Noise is a critical parameter influencing the performance of the PZR sensor, particularly in the

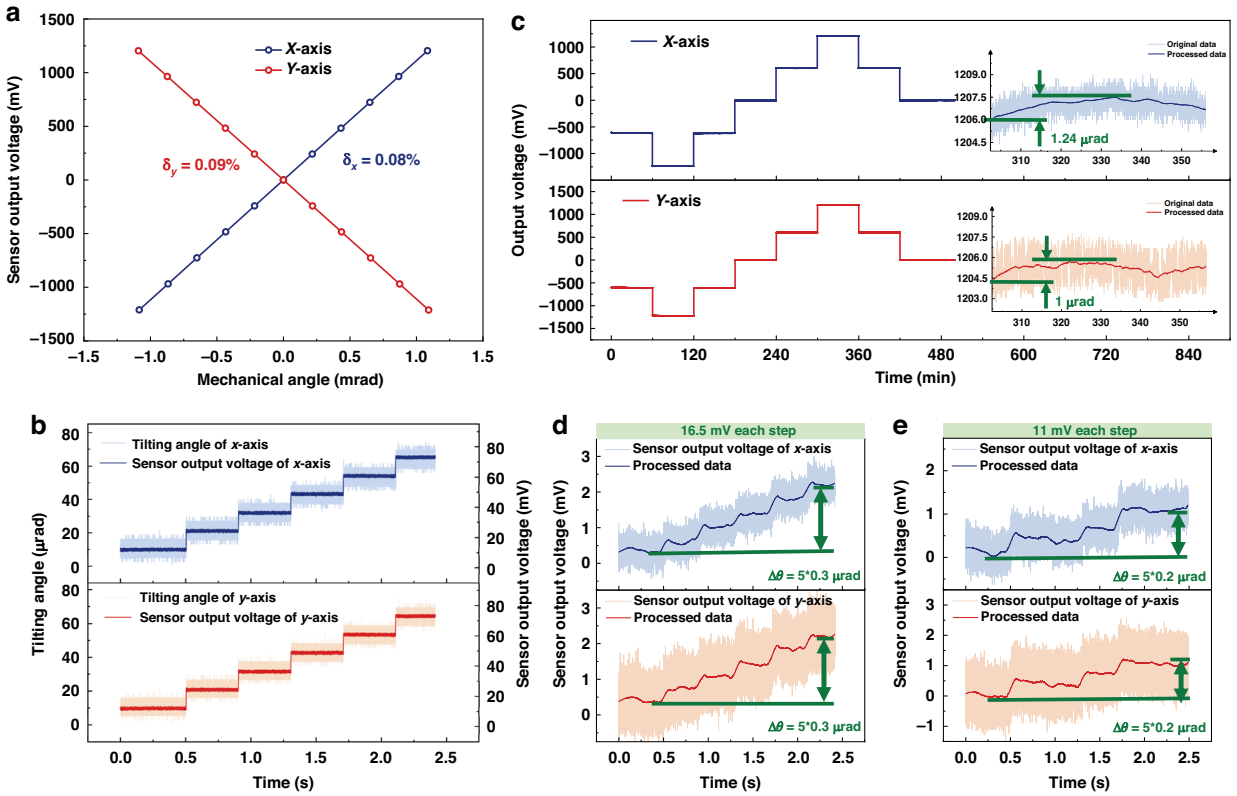

Fig. 5 The test results of the PZR sensor. a Linearity of piezoresistive sensor at half scale (± 55 V); **b** synchronism of mechanical angle and the output voltage of piezoresistive sensor; **c** piezoresistive output stability; **d** angular resolution of the PZR sensor at 16.5 mV each step of FSM; and **e** angular resolution of the PZR sensor at 11 mV each step of FSM

characterization of angular resolution. Our testing system has an inherent noise level of approximately 1.25 mV. If the PZR output signal is not amplified, this system noise corresponds to an angle of 104 μrad. In the case of small-angle operational states, the PZR signal is significantly obscured by the noise. To achieve a smaller angular resolution, the supply voltage and amplification factor are adjusted to minimize noise in the output signal. The PZR supply voltage is set to 1.2 V, and the PZR output voltage is amplified by a factor of 200. Consequently, the noise of the sensor output voltage is about 2.2 mV, which is equal to 1.8 μrad. Figure 5 presents the performance of the PZR sensors of the MEMS FSM. The PZR output signal is collected by a data acquisition card and recorded by the computer. In Fig. 5a, we obtain the relationship between the output voltage of the PZR sensor and the deflection angle. A sequence of DC voltages ranging from −55 V to +55 V, with increments of 11 V, is applied to the FSM. The nonlinearity observed between the sensor signal and the deflection angles for the *x*-axis and *y*-axis is measured at 0.08% and 0.09%, respectively, based on the half-scale range of ±55 V for the device. The sensitivity is calculated to be 5.036 mV/(V·mrad) for the *x*-axis and 5.024 mV/(V·mrad) for the *y*-axis, which shows favorable agreement with the simulation result and proves that the SCR can effectively improve the sensitivity. Figure 5b characterizes the synchronism between the sensor output and the deflecting angle of the FSM. A stepped waveform voltage of 550 mV each step is given to actuate the mirror, while the deflection angle and the corresponding output signal from the PZR sensor are simultaneously recorded. The result shows a good synchronism between the voltage output of the sensor and the angle. Figure 5c depicts the stability test of the PZR sensor, where both axes are individually driven through the following sequence of voltages: −27.5 V, −55 V, −27.5 V, 0 V, 27.5 V, 55 V, 27.5 V, and 0 V, with each voltage maintained for 1 h. The recorded PZR output signals reveal that, after amplifying the resistive signal under a 55 V drive, the maximum fluctuations observed within this hour were 1.24 μrad for the *x*-axis and 1 μrad for the *y*-axis. Figure 5d, e shows the results of the angular resolution test of the PZR sensor. As shown in Fig. 5d, the minimum angular resolution of the resistive sensor is 0.3 μrad@16.5 mV. Figure 5e demonstrates that at a lower driving voltage of 11 mV, the resistive sensor fails to respond adequately to every step change.

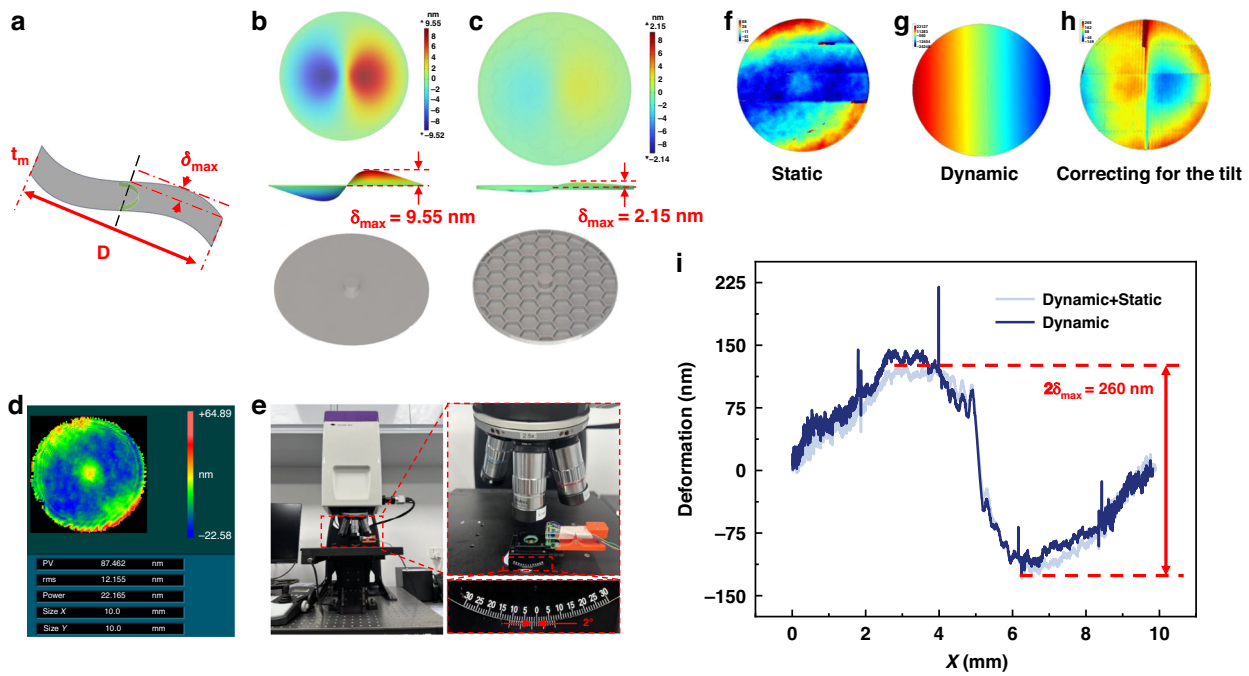

Fig. 6 The characterization of mirror dynamic deformation. a Schematic diagram of mirror dynamic deformation; **b** FEA simulation of dynamic deformation of equivalent mass mirror model (2 mrad@500 Hz); **c** FEA simulation of dynamic deformation reinforced mirror model (2 mrad@500 Hz); **d** static deformation of the mirror tested by a Fizeau interferometer; **e** the experimental setup for dynamic deformation measurement; **f** Static deformation of the mirror tested by DHM; **g** topography recorded by DHM; **h** correcting for the tilting angle; and **i** subtracting static deformation, resulting dynamic deformation

Dynamic deformation of the mirror plate

The rapid motion of the MEMS FSM results in dynamic deformation of the mirror surface, as shown in Fig. 6a. This dynamic deformation, defined as the deviation from linearity, can be predicted using Brosens's formula below, which uses the unevenly distributed forces due to acceleration across the mirror surface[24].

$$\delta_{\max} = 0.217 \frac{\rho f^2 D^5 \theta_{mech}}{E t_m^2} \tag{4}$$

where ρ is the material density, E is the modulus of elasticity, f is the scanner frequency, D is the mirror aperture, θ_{mech} the mechanical tilting angle, and t_m is the mirror thickness. To keep the spot diffraction limited, the maximum mechanical mirror deformation ($\delta_{\max}$) should not exceed λ/10 of the shortest system wavelength[25].

To enhance resistance to static deformation, we optimized the rib shapes and sizes while maintaining the same mirror mass, and ultimately, we selected a honeycomb-shaped reinforcement structure for the mirror[18]. Figure 6d shows the static deformation of our mirror measured by a Fizeau interferometer (Zygo Verifire interferometer, America). The average PV value and RMS value of the surface figure of the devices are 87 nm and 12 nm. It is worth noting that the RMS value is merely λ/120 (λ = 1550 nm). In addition, the reinforcement structure of the mirror also contributes to reducing dynamic deformation. Figure 6b, c shows the dynamic deformation simulation results for the dynamic deformation of the mirror subjected to a tilting angle of 2 mrad at a frequency of 500 Hz. The reinforced mirror exhibits a maximum dynamic deformation of 2.15 nm, whereas the equivalent mass pure mirror model demonstrates a significantly higher maximum dynamic deformation of 9.55 nm. Here, the dynamic deformation of the equivalent mass pure mirror model can be calculated using Eq. (4), where $\theta_{\text{mech}} = 2$ mrad, $f = 500$ Hz, $t_m = 121$ μm, $E = 170 \times 10^9$ Pa, $\rho = 2329$ kg/m^3, and $D = 10$ mm. The calculated dynamic deformation $\delta_{\max}$ is 10.15 nm, which aligns closely with the simulation result of 9.55 nm, thereby validating the accuracy of the simulation model. The simulation and theoretical calculation results indicate that the reinforced structure effectively reduces dynamic deformation by a factor of four compared to the unreinforced model.

Currently, there is a limited amount of experimental research on dynamic deformation. Earlier studies measured dynamic deformation using LDV[26], phase shifting interferometry[27], and Shack–Hartmann wavefront sensor (SHWS)[28]. These approaches rely on manual point measurements or offer poor lateral resolution, and they are

primarily designed for dynamic deformation measurement of small mirrors (less than 2 mm in size). Recently, Silicon Austria Labs GmbH presented an approach using digital holographic microscopy (DHM)[29], which has high nanometric vertical resolution and, compared to SHWS, much higher lateral resolution, to measure the dynamic deformation of a 2 mm resonating piezoelectric MEMS mirror. In this paper, we also use the DHM R2100 from Lyncée Te, to measure the dynamic deformation of the MEMS FSM. The measurements are performed using an objective with a magnification of 2.5×, an NA of 0.07, and a field of view of 2.64 mm. As our 10 mm mirror plate is far beyond the field of view, a stitching mode is needed to measure such a big mirror. Figure 6f is the topography of the mirror stitched by DHM at a static state. The surface topography of the FSM is basically the same as that measured by the Fizeau interferometer. According to the simulation result, under a quasi-static state (2 mrad@500 Hz), the dynamic deformation is only 2.15 nm, and the surface topography of the mirror remains largely consistent with its static state. The dynamic deformation will be submerged in its own static deformation and system test noise. Therefore, we choose to measure the frequency near the resonance region while the mirror tilts at larger angles, where the mirror produces a more pronounced dynamic deformation.

According to the simulation result, the maximum dynamic deformation of the mirror of 35 mrad (2°) @1108 Hz is 181 nm. This value exceeds that of the static deformation and the system noise and can be measured by DHM. However, the vertical height of the mirror is higher than 300 μm, which is larger than the maximum measurable vertical height attainable by DHM. Therefore, a goniometer is needed[29], as shown in Fig. 6e, to manually adjust the angle of the micromirror so that the FSM is exactly perpendicular to the objective lens at 2° so that the vertical height difference across the mirror is within holographically measurable limits. Figure 6g shows the deformation map of the mirror at 1108 Hz. The mirror has a slight angle (4 mrad) relative to the objective plane. As shown in Fig. 6h, a plane is fitted to the deformation map, and this residual tilt angle is added to the set angle of the goniometer to obtain a final tilt angle of 31 mrad. Figure 6i gives the maximum dynamic deformation of the mirror of 31 mrad at 1108 Hz is 130 nm, which is basically consistent with the simulation value of 161 nm. We can infer that the dynamic deformation of our MEMS FSM is less than 2 nm in the quasi-static state by characterizing the dynamic deformation under a large angle around the resonant frequency. The low dynamic deformation effectively minimizes signal loss due to beam deviations, thereby improving communication reliability.

Reliability

Evaluating long-term stability is crucial for the FSM due to its intended application in space environments. Based on accelerated lifetime testing and environmental simulations, several experiments have been conducted to evaluate the long-term stability of the MEMS FSM under conditions relevant to space applications. Firstly, to evaluate mechanical fatigue resistance, the FSM has been operated continuously for 30 billion cycles within a full range of ±2 mrad at a frequency of 600 Hz under normal temperature and pressure conditions. Remarkably, no changes were observed in the resonant frequency or tilting angle throughout this testing period. As single-crystal silicon (Si) is a brittle material, its fracture behavior is closely associated with its fracture strength. Within the permissible stress limits, Si-based MEMS devices exhibit excellent fatigue resistance characteristics. Additionally, considering the long-term exposure to space conditions such as radiation and temperature variations. The devices underwent temperature cycling between −40 °C and 100 °C at a rate of 1 °C/min for 23.5 cycles. Due to the high-temperature resistance characteristics of Si and AlScN[30], the results demonstrated that both the resonant frequency and tilting angle changed less than 1%. Furthermore, to assess resilience to gamma radiation exposure, the devices were subjected to a total dose of 150 krad (Si) at a dose rate of 15 rad (Si)/s. Due to the radiation stability of Si and AlScN, the resonant frequency and tilting angle exhibited changes of less than 0.1%, and the actuator capacitance showed similar stability with less than 0.1% variation.

Discussion

Upon completion of the aforementioned tests, we can assert that all parameters of our FSM are consistent with the stringent requirements necessary for laser ISLs. Here, we conducted a comparative analysis of the key parameters of various FSMs as shown in Table 2. The selected parameters are specifically relevant to the applications in laser ISLs as mentioned in the introduction. This comparison includes typical traditional FSMs (piezoelectric ceramic FSM S-331.2[31] from PI and voice coil motor FSM from TNO[32]), as well as MEMS FSMs that have already been employed in laser ISLs (Mirrorcle Technologies A5L2.2[33] and Hamamatsu S1227-03P[34]). Our FSM exhibits reduced dimensions that align more effectively with the SWaP principles compared to traditional FSMs. In contrast to other MEMS FSMs, our mirror features a larger mirror size and a higher resonant frequency. The increased mirror size enhances the optical throughput in ISLs. Also, the higher resonant frequency minimizes latency during rapid beam realignment. In addition, our FSM stands out for its lowest nonlinearity and step response time. Therefore, complex compensation algorithms are not required due to the high linearity, decreasing computational overhead. The low step response time of 0.8 ms ensures precise tracking of

Table 2 Comparison of FSMs by key criteria

Research institution	Ref. [31]	Ref. [32]	Ref. [33]	Ref. [34]	This work
Type	Piezoelectric ceramic FSM	Voice coil motor FSM	Electrostatic MEMS FSM	Electromagnetic MEMS FSM	Piezoelectric MEMS FSM
Size (mm^3)	14726	13253	484	540	1716
Mirror size (mm)	12.7	20	7.5	2.6	10
Maximum mechanical angle (mrad)	±2.1	±17.4	±21	±130	±2.1
Resonant frequency (Hz)	9000	3600	559	530	1230
Nonlinearity	0.3%	No data	>1%	1.3%	0.05%
Angular resolution (μrad)	0.05	50	No data	No data	0.3
Repeated accuracy (μrad)	3	1	No data	No data	1.11
Step response (ms)	4	1	4	2	0.41
Integrated angle sensor	Assembled	Assembled	No	No	Integrated

satellite platform jitter. Also, we have a quite high level of angular resolution and repeatability accuracy, ensuring precise beam direction.

Additionally, the COTS FSMs discussed here require separate feedback modules, complicating system architecture and increasing power consumption. In contrast, our FSM integrated with PZR sensors adopts an SOI fabrication process that is compatible with CMOS technology. This approach reduces both system complexity and overall footprint, making it more suitable for compact optical systems. Furthermore, the integration of PZR sensors minimizes the need for additional external sensor components, potentially lowering overall system costs.

Conclusion

This paper introduces a compact, high-performance piezoelectric MEMS FSM integrated with PZR sensors tailored for laser ISLs. The mirror features a substantial optical aperture of 10 mm and a packaged volume of $26 \times 22 \times 3\ mm^3$. A novel intermediate directional defect structure is implemented to create an SCR, resulting in a 63% increase in the piezoresistive sensitivity from 3.3 mV/(V·mrad) to 5.4 mV/(V·mrad). The performance evaluation of the FSM encompasses various metrics, including mechanical properties, the PZR sensor characteristics, and mirror optical quality—all of which align with laser ISLs requirements. Results reveal that the FSM achieves a resonant frequency exceeding 1 kHz and exhibits low nonlinearity at 0.05% within a range of ±2.1 mrad. Remarkably, it provides a minimum angular resolution of 0.3 μrad and repeatable positioning accuracy of 1.11 μrad, ensuring superior pointing precision. A control bandwidth of 2038 Hz is achieved through a double-step algorithm. Furthermore, the integrated angular sensor displays a nonlinearity of 0.09% at ±1.08 mrad, a sensitivity of 5.1 mV/(V·mrad), and maintains a minimum angular resolution of 0.3 μrad. Under quasi-static driving conditions (500 Hz at ±2 mrad), the maximum dynamic deformation of the mirror surface is limited to just 2 nm. The future work will focus on the development of the MEMS FSM with a larger mirror plate to provide a broader capturing field of view for laser ISLs. Further, the closed-loop control will be employed to achieve higher accuracy.

Acknowledgements
The authors acknowledge the support from the National Key Research and Development Program of China (no. 2023YFB3209900).

Author details
[1]State Key Laboratory of Transducer Technology, Shanghai Institute of Microsystem and Information Technology, Chinese Academy of Sciences, Shanghai, China. [2]University of Chinese Academy of Sciences, Beijing, China. [3]Shanghai Industrial μTechnology Research Institute, Shanghai, China. [4]MExpert Technologies Co. Ltd, Shanghai, China. [5]School of Microelectronics, Shanghai University, Shanghai, China. [6]School of Information Science and Technology, ShanghaiTech University, Shanghai, China

Competing interests
The authors declare no competing interests.

Supplementary information The online version contains supplementary material available at https://doi.org/10.1038/s41378-025-00935-1.

Received: 10 December 2024 Revised: 13 February 2025 Accepted: 9 March 2025
Published online: 29 April 2025

References

1. Carlos, C., Markus, K., Joachim, H., Diaz, G. D. & Paul, C. Optical inter-satellite link terminals for next generation satellite constellations. *Proc. SPIE* **11272**, 1127203, https://doi.org/10.1117/12.2545629 (2020).
2. Kaushal, H. & Kaddoum, G. Optical communication in space: challenges and mitigation techniques. *IEEE Commun. Surv. Tutor.* **19**, 57–96, https://doi.org/10.1109/COMST.2016.2603518 (2017).

3. Lee, K., Mai, V. & Kim, H. Acquisition time in laser inter-satellite link under satellite vibrations. *IEEE Photon. J.* **15**, 1–9, https://doi.org/10.1109/JPHOT.2023.3291807 (2023).
4. Li, Q. et al. Development of multitarget acquisition, pointing, and tracking system for airborne laser communication. *IEEE Trans. Ind. Inform.* **15**, 1720–1729, https://doi.org/10.1109/TII.2018.2868143 (2019).
5. Ryan, M. et al. Implementation of laser communications acquisition function using MEMS FSM and quad detector. *Proc. SPIE* **11993**, 1199302, https://doi.org/10.1117/12.2606010 (2022).
6. Shinshi, T. et al. A fast steering mirror using a compact magnetic suspension and voice coil motors for observation satellites. *J. Micromech. Microeng.* **30**, 094001, https://doi.org/10.3390/electronics9121997 (2020).
7. Zhou, Z. et al. Single preloaded piezoelectric-ceramic-stack-actuator-based fast steering mirror with an ultrahigh natural frequency. *Appl. Opt.* **59**, 3871–3877, https://doi.org/10.1364/AO.387262 (2020).
8. Kammerer, W. et al. CLICK-A: Optical communication experiments from a CubeSat downlink terminal. In *Proc. AIAA/USU Conf. Small Satell., SSC23-WVII-04 (2023). Available via DigitalCommons@USU—Small Satellite Conference: CLICK-A: Optical Communication Experiments From a CubeSat Downlink Terminal.*
9. Grenfell, P. et al. Design and prototyping of a nanosatellite laser communications terminal for the CubeSat Laser Infrared CrosslinK (CLICK) B/C mission. In *Proc. AIAA/USU Conf. Small Satell., SSC20-WKVI-02* (Small Satellite, Logan, 2020); https://digitalcommons.usu.edu/smallsat/2020/all2020/37
10. Cahoy, K. L. & Čierny, O. On-orbit beam pointing calibration for nanosatellite laser communications. *Opt. Eng.* **58**, 041605, https://doi.org/10.1117/1.OE.58.4.041605 (2018).
11. Taylor, M. et al. Polar orbiting infrared tracking receiver POINTR. *J. Spacecr. Rockets* **56**, 1–13, https://doi.org/10.1109/AERO.2019.8741738 (2019).
12. Ishola, F. & Cho, M. Experimental study on photodiode array sensor aided MEMS fine steering mirror control for laser communication platforms. *IEEE Access* **9**, 100197–100207, https://doi.org/10.1109/ACCESS.2021.3096816 (2021).
13. Milaševičius, M. & Mačiulis, L. A review of mechanical fine-pointing actuators for free-space optical communication. *Aerospace* **11**, 5, https://doi.org/10.3390/aerospace11010005 (2024).
14. Edward, H. *Control of a Fast Steering Mirror for Laser-Based Satellite Communication* (Massachusetts Institute of Technology, 2006); http://hdl.handle.net/1721.1/35672
15. Coppoolse, W. et al. Dual-axis single-mirror mechanism for beam steering and stabilisation in optical inter-satellite links. *ESA Spec. Publ.* **524**, 183–190 (2003).
16. Pain, T. et al. Beam steering mechanism for EarthCARE atmospheric lidar instrument ATLID: An ultra-stable piezoelectric tip-tilt mechanism,. *Proc. SPIE* **10233**, 31001, https://doi.org/10.1117/12.2296059 (2017).
17. Liu, Y. et al. A MEMS fast steering mirror with 10 mm aperture for free-space optical communication. *IEEE 37th Int. Conf. Mems.* **10**, 1011–1014, https://doi.org/10.1109/MEMS58180.2024.10439423 (2024).
18. Yang, Y. et al. MEMS fast steering mirror with a large optical aperture and high surface quality for free-space optical communication. *Opt. Express* **32**, 37932–37945, https://doi.org/10.1364/OE.525126 (2024).
19. Zhang, H. et al. Process control monitor (PCM) for simultaneous determination of the piezoelectric coefficients d31 and d33 of AlN and AlScN thin films. *Micromachines* **13**, 581, https://doi.org/10.3390/mi13040581 (2022).
20. Yang, W. et al. Piezoelectric MEMS fast steering mirror with high reliability for free-space laser communication. *Proc. SPIE*. https://doi.org/10.1117/12.3000029 (2024).
21. Kumar, S. S. & Pant, B. D. Design principles and considerations for the 'ideal' silicon piezoresistive pressure sensor: a focused review. *Microsyst. Technol.* **20**, 1213–1247, https://doi.org/10.1007/s00542-014-2215-7 (2014).
22. Tanaskovic, D., Djuric, Z. & Lazic, Z. Influence of impurity distribution on thermal coefficients of resistivity and piezoresistivity of diffused layers in silicon. In: *Proceedings of International Conference on Microelectronics.* **4**, 573–576, (1995); https://doi.org/10.1109/ICMEL.1995.500929
23. Li, A. N. et al. Determination of crosstalk in a dual-axis piezoelectric MEMS mirror and suppression with feedforward algorithms. *IEEE Sens. J.* **24**, 32272–32282, https://doi.org/10.1109/JSEN.2024.3447905 (2024).
24. Holmstrom, S. T. S., Baran, U. & Urey, H. MEMS laser scanners: a review. *J. Microelectromech. Syst.* **23**, 259–275, https://doi.org/10.1109/JMEMS.2013.2295470 (2014).
25. Urey, H., Wine, D. W. & Osborn, T. D. Optical performance requirements for MEMS-scanner based microdisplays. *Proc. SPIE* **4178**, 176–185, https://doi.org/10.1117/12.396486 (2000).
26. Ji, C. H. et al. An electrostatic scanning micromirror with diaphragm mirror plate and diamond-shaped reinforcement frame. *J. Micromech. Microeng.* **16**, 1033–1039, https://doi.org/10.1088/0960-1317/16/5/021 (2006).
27. Hsu, S. et al. Fabrication and characterization of a dynamically flat high-resolution micro-scanner. *J. Opt. A Pure Appl. Opt.* **10**, 044005, https://doi.org/10.1088/1464-4258/10/4/044005 (2008).
28. Margaret, K. B. et al. Measurement of the dynamic deformation of a high-frequency scanning mirror using a Shack–Hartmann wavefront sensor. *Proc. SPIE* **4451**, 480–488, https://doi.org/10.1117/12.453645 (2001).
29. Thakkar, P. et al. Measuring angle-resolved dynamic deformation of micro-mirrors with digital stroboscopic holography. *Proc. SPIE*. https://doi.org/10.1117/12.2621325 (2022).
30. Gao, C. et al. Investigation of thermal annealing on the characteristics of Sc Al1—N thin films. *Vacuum*. https://doi.org/10.1016/j.vacuum.2023.112669 (2023).
31. High-Speed Tip/Tilt Platform (Datasheet). *Physik Instrumente*. https://www.pi-usa.us/fileadmin/user_upload/physik_instrumente/files/datasheets/S-331-Datasheet.pdf (2024).
32. Kuiper, S. et al. *High-Bandwidth and Compact Fine Steering Mirror Development for Laser Communications* (ESMATS, 2017).
33. Gimbal-Less Two-Axis Scanning MEMS Micromirrors (Datasheet). *Mirrorcle Technologies*. https://www.mirrorcletech.com/pdf/DS/MirrorcleTech_Datasheet_A5L2.2-7500AU_S46749.pdf (2020).
34. Ultra-Miniature. *High-Performance Electromagnetically Driven Laser Scanning MEMS Mirror (Datasheet), Hamamatsu Photonics*. https://www.hamamatsu.com.cn/content/dam/hamamatsu-photonics/sites/documents/99_SALES_LIBRARY/ssd/s12237-03p_koth1006e.pdf (2023).